Sensitivity of Arctic clouds to ice microphysical processes in the NorESM2 climate model

Georgia Sotiropoulou[1,2,3], Anna Lewinschal[2], Paraskevi Georgakaki[3], Vaughan Phillips[4], Sachin Patade[4], Annica M. L. Ekman[2], Athanasios Nenes[1,3]

[1]ICE-HT, Foundation for Research and Technology Hellas (FORTH), Patras, Greece
[2]Department of Meteorology, Stockholm University & Bolin Center for Climate Research, Sweden
[3]Laboratory of Atmospheric Processes and their Impacts (LAPI), Ecole Polytechnique Fédérale de Lausanne (EPFL), Lausanne, Switzerland
[4]Department of Physical Geography, University of Lund, Lund, Sweden

Corresponding author: georgia.sotiropoulou@epfl.ch , athanasios.nenes@epfl.ch

Keywords: ice formation, secondary ice production, ice multiplication, Arctic clouds, climate models, Arctic radiation budget

Abstract

Ice formation remains one of the most poorly represented microphysical processes in climate models. While primary ice production (PIP) parameterizations are known to have a large influence on the modeled cloud properties, the representation of secondary ice production (SIP) is incomplete and its corresponding impact is therefore largely unquantified. Furthermore, ice aggregation is another important process for the total cloud ice budget, which also remains largely unconstrained. In this study we examine the impact of PIP, SIP and ice aggregation on Arctic clouds, using the Norwegian Earth System model version 2 (NorESM2). Simulations with both prognostic and diagnostic PIP show that heterogeneous freezing alone cannot reproduce the observed cloud ice content. The implementation of missing SIP mechanisms (collisional break-up, drop-shattering and sublimation break-up) in NorESM2 improves the modeled ice properties, while improvements in liquid content occur only in simulations with prognostic PIP. However, results are sensitive to the description of collisional break-up. This mechanism, which dominates SIP in the examined conditions, is very sensitive to the treatment of the sublimation correction factor, a poorly-constrained

parameter that is included in the utilized parameterization. Finally, variations in ice aggregation treatment can also significantly impact cloud properties, mainly through its impact on collisional break-up efficiency. Overall, enhancement in ice production though the addition of SIP mechanisms and the reduction of ice aggregation (in line with radar observations of shallow Arctic clouds) result in enhanced cloud cover and decreased TOA radiation biases, compared to satellite measurements, especially during the cold months.

Significance

Arctic clouds remain a large source of uncertainty in projections of the future climate due to the poor representation of the microphysical processes that govern their life cycle. Ice formation is among the least understood processes. While it is widely recognized that better constraints on primary ice production (PIP) are needed to improve existing parameterizations, we show that secondary ice production (SIP) and ice aggregation can have also a significant impact on the ice number concentrations. Constraining ice formation through the addition of missing SIP mechanisms and reducing ice aggregation can improve the representation of the cloud macrophysical properties and enhance total cloud cover in the Arctic region, which in turn contributes to decreased TOA radiation biases in the cold months.

1. Introduction

Clouds and cloud feedbacks remain the largest source of uncertainty in predictions of the future climate (Boucher et al. 2013). In the most recent Climate Model Intercomparison Project (phase 6 – CMIP6) many general circulation models (GCMs) exhibited larger sensitivity to changes in carbon dioxide concentrations, a metric known as Equilibrium Climate Sensitivity (ECS), compared to CMIP5 models (Zelinka et al. 2020). Murray et al. (2021) showed that ECS values in CMIP6 correlate with mid-to-high latitude low-level cloud feedbacks. Moreover, CMIP6 models suffer from biases in high-latitude cloud cover (Vignesh et al. 2020), cloud radiative impacts (Sledd and L'ecuyer 2020) and snowfall patterns (Thomas et al. 2019).

Mixed-phase clouds, consisting of both supercooled liquid and ice, are the most abundant Arctic cloud type at temperatures between -25^{o}C and 0^{o}C (Shupe et al. 2006; 2011). While these clouds are theoretically thermodynamically unstable and can easily glaciate through the Wegener-Bergeron-Findeisen (WBF) mechanism, they have been observed to persist for days to weeks (Morrison et al. 2012). Moreover, as ice crystals grow through vapor

deposition, they can start forming aggregates through collisions with other ice particles or they can gain mass through the collection of liquid droplets (i.e. riming) until they eventually fall out in the form of snow or graupel. Mixed-phase cloud observations often indicate that the supercooled liquid layer is concentrated near cloud top with ice particles falling below, which allows the liquid phase to be maintained (Morrison et al. 2012). Modeling the life-cycle of these clouds is challenging since errors in the representation of the complex processes that maintain them can lead to rapid glaciation. At the same time a correct representation of the vertical structure and cloud phase is crucial for an accurate estimation of the cloud radiative impact (Curry et al. 1996). Predictions of Arctic warming are particularly sensitive to cloud ice formation (Tan et al. 2019). While ice formation processes are likely an important contributor to the CMIP6 spread in predicted mid- and high-latitude cloud feedbacks (Murray et al. 2021), they remain among the most poorly understood microphysical processes in mixed-phase clouds (Seinfeld et al. 2016; Storelvmo 2017).

Primary ice production (PIP) at temperatures above -38^{o}C can only happen heterogeneously in the atmosphere, which means that the assistance of insoluble aerosols that act as Ice Nucleating Particles (INPs) is required (Hoose and Möhler 2012). However, primary ice crystal concentrations can further be enhanced through multiplication processes (Field et al. 2017; Korolev and Leisner 2020), known as secondary ice production (SIP). SIP has received substantially less attention than PIP in the past decades, which is the reason behind its poor (or absent) representation in atmospheric models. Several observational (Gayet et al. 2009; Lloyd et al. 2015; Luke et al. 2021; Pasquier et al. 2022) and modeling (Sotiropoulou et al. 2020; 2021b; Zhao et al. 2021; Zhao and Liu 2021; 2022) studies have indicated that SIP might be particularly important for Arctic clouds, as INP concentrations in the Arctic region are generally low (Wex et al. 2020) to account for the high ice crystal number concentrations (ICNCs) observed (Hobbs and Rangno 1998).

Several mechanisms that can trigger ice multiplication have been identified in laboratory experiments (Korolev and Leisner 2020), however only one SIP mechanism has until now been considered in GCMs: the Hallett-Mossop (HM) process (Hallett and Mossop, 1974). This is also the case for the Norwegian Earth System model version 2 (NorESM2), which allows HM to occur after cloud drop-snow collisions. However, observational (Rangno and Hobbs 2001; Schwarzenboeck et al. 2009; Luke et al. 2021) and modeling studies (Sotiropoulou et al. 2020; 2021b; Zhao et al. 2021; Zhao and Liu 2021; 2022) suggest that other SIP processes, like collisional break-up (Vardiman 1978; Takahashi et al. 1995) and

drop-shattering (Lauber et al. 2018; Keinert et al. 2020), also have a significant influence on Arctic cloud microphysical structure.

In this study we implement descriptions for drop-shattering (DSH) and collisional break-up (BR) in NorESM2, using parameterizations from the recent literature (Phillips et al. 2017a,b; 2018). We further test the efficiency of sublimation break-up (SUBBR) (Oraltay and Hallett 1989; Bacon et al. 1998), a process whose efficiency remains unknown in Arctic atmospheric conditions, using the parameterization developed by Deshmukh et al. (2022). In addition, we modify the existing HM description to further account for rain-snow collisions. Sensitivity simulations with varying PIP, SIP and ice aggregation treatment are conducted to quantify the ice-related processes that are most impactful on ice particle number. Results are initially evaluated against two-year surface-based observations from Ny-Ålesund for the period June 2016 - May 2018 to assess the most realistic simulation set-up. Satellite radiation and cloud measurements are further used to quantify the impact of the examined processes on the current climate state over the whole Arctic region.

2. Methods

a. Observations

Field observations of clouds were collected at Ny-Ålesund in 2016–2018 in the context of the Arctic Amplification: Climate Relevant Atmospheric and Surface Processes, and Feedback Mechanisms $(AC)^3$ project. With the addition of a W-band cloud radar, this observation site became one of the few Arctic sites capable of state-of-the-art long-term cloud profiling with high temporal and spatial resolution. A detailed analysis of the observed cloud properties is offered by Nomokonova et al. (2019; 2020). The total occurrence of clouds was found to be ~81%. The most predominant type of clouds was multi-layer clouds with a frequency of occurrence of 44.8%. Single-layer clouds occurred 36%, with the vast majority of them being mixed-phase; liquid hydrometeors were generally observed within the lowest two kilometers in the atmosphere.

Below the measurements utilized to evaluate the model are described. Macro- and micro- physical cloud properties are derived from a combination of instruments that includes a 94 GHz cloud radar, a ceilometer and a HATPRO radiometer (Nomokonova et al. 2019d). The cloud Liquid water path (LWP) is derived from a HATPRO microwave radiometer

(Nomokonova et al. 2019a,b,c) with typical uncertainty around +/- 20–25 g m^{-2}, using a multivariate linear regression algorithm developed at the University of Cologne (Löhnert and Crewell 2003). HATPRO cannot provide reliable estimates under rainy conditions, when the instrument radome becomes wet. Such periods have been identified and excluded from the analysis, using the instrument's precipitation sensor. Thermodynamic variables such as temperature (Nomokovova et al. 2019d,e,f) and integrated water vapor (IWV; Nomokovova et al. 2019g,h,i) are also derived from HATPRO.

Once the Cloudnet retrieval algorithm (Illingworth et al. 2007) has been applied to categorize the measured particles as liquid droplets, ice, melting ice, and drizzle/rain, ice water content (IWC) is derived from radar reflectivity and temperature measurements following the methodology of Hogan et al. (2006). The uncertainties in this IWC retrieval range from -33% to +50% for temperatures above -20°C and from -50% to +100% for temperatures below -40°C. The effective radius of ice particles (r_{ieff}) is calculated following Delanoë and Hogan (2010), using IWC and visible extinction coefficient estimates (Ebell et al. 2020); the latter is also derived following Hogan et al. (2006). The uncertainty in r_{ieff} retrieval described by Delanoë and Hogan (2010) is about 30%, while the uncertainty for the radar-derived visible extinction coefficient that is used in the ice effective radii retrieval is 62% to 160% (Hogan et al. 2006). de Boer et al. (2009) reported that assumptions in the shape of ice particles might result in a 200 μm uncertainty in r_{ieff} estimations that are based on cloud radar and lidar techniques.

Surface in-situ cloud measurements were collected at the Zeppelin station, on mount Zeppelin near Ny-Alesund town, with the Zeppelin Observatory counterflow virtual impactor (CVI) inlet (Karlsson et al. 2021a,b) for a similar period (until February 2018) as the remote sensing observations. However, this instrument samples only small cloud particles with diameters below 50 μm, thus it cannot be used for the evaluation of the whole modeled cloud particle spectrum.

Finally, since Ny-Alesund conditions differ from those observed at other pan-Arctic sites and in the central Arctic, in terms of both thermodynamic (e.g. Naaka et al. 2018) and aerosol (e.g. Schmeisser et al. 2018) properties, this is expected to lead in a variable impact of the examined processes across the Arctic. For this reason, local measurements are complemented with satellite datasets to evaluate the modeled radiation and cloud characteristics over the whole Arctic region. These include the Clouds and Earth's Radiant Energy Systems (CERES; Wielicki et al. 1996) Energy Balanced and Filled (EBAF) product,

edition 4.1 (Kato et al. 2018) and the GCM-Oriented CALIPSO Cloud Product (GOCCP) Version 3 (Chepfer et al. 2010).

b. Model description

For our investigations we use the NorESM2-MM version (Selund et al. 2021) with 1^{o} horizontal resolution (development branch). Wind and pressure fields are nudged towards ERA-Interim profiles to limit the influence of meteorological errors on microphysical fields. The relaxation time for nudging is set to 6 hours, same as the time resolution of the reanalysis data (Dee et al. 2011). Simulations are run for 29 months, from 1 January 2016 to 31 May 2018, with fixed sea-surface temperatures (SSTs). The first five months are considered as spin-up, while the rest of the data are used for comparison with surface-based observations from Ny-Ålesund. A description of the modeled ice microphysics, which is the main focus of this study, and the implemented modifications follow below.

The atmospheric component of NorESM2 is CAM6-Oslo, which consists of the Community Atmosphere Model version 6 (CAM6) and the OsloAero5.3 (Kirkevåg et al. 2018) aerosol scheme. CAM6-Oslo employs the Morrison and Gettelman (2015) microphysics scheme (MG2), which accounts for four hydrometeor types: cloud droplet, raindrop, cloud ice and snow. Heterogeneous PIP parameterizations follow the Classical Nucleation Theory (CNT; Hoose et al. 2010; Wang et al. 2014) which accounts for immersion, contact and deposition freezing of two INP species, dust and soot. Immersion freezing is only allowed to occur below -10^{o}C in this scheme for both INP species, while only 10% of the soot concentrations are considered efficient INPs. While CNT is the default nucleation scheme used in CMIP6, the model employs an alternative option for PIP: CNT can be replaced by diagnostic parameterizations that are a function of basic thermodynamic variables and do not account for explicit cloud-aerosol interactions. These include the Bigg (1953), Young (1974) and Meyers et al. (1992) parameterizations for immersion, contact and deposition freezing, respectively. The Bigg (1953) and Young (1974) parameterizations are activated at temperatures below -4^{o}C, while Meyers et al. (1992) is active within the -37^{o}C–0^{o}C temperature range.

Secondary ice production is accounted in MG2 scheme only through the HM mechanism, which is parameterized following Cotton et al. (1986). This formulation considers a maximum splinter production of 350 splinters per milligram of rime at -5^{o}C, while the process efficiency decreases to zero at temperatures below (above) -8^{o}C (-3^{o}C). However,

HM is only activated after cloud droplets collide with snow; in our modified code, we further account for the contribution from raindrop-snow collisions, following Morrison et al. (2005) scheme, using the same parameterization (Cotton et al. 1986) for the prediction of the generated fragments. Estimations of mass and number collision tendencies for raindrop-snow collisions are available in the standard MG2 scheme.

To represent the BR mechanism, we implement the parameterization of Phillips et al. (2017a). The process is initiated after snow particles collide with each other or with cloud ice. We assume that the collisions that do not result in sticking (aggregation) at an instant timestep, can bounce to initiate the break-up. Phillips et al. (2017a) is a physically-based parameterization that predicts the number of generated fragments as a function of collisional kinetic energy, while the effect of the colliding particles' size, rimed fraction and ice habit is further accounted. MG2 however does not predict rimed fraction and ice habit. For this reason, in our simulations planar ice particles with a 0.4 rimed fraction are assumed; planar shape accounts for a larger range of shapes and is valid for a wider temperature range, while a high fraction has been shown to give the most optimal results in simulations of polar clouds (Sotiropoulou et al. 2020; 2021a). All generated fragments from this mechanism are added to the cloud ice category.

The DSH description follows Phillips et al. (2018) and is initiated after raindrop-INP (immersion freezing), raindrop-snow and raindrop-ice collisions. For ice multiplication due to raindrop-INP and raindrop-cloud ice collisions we utilize the formulation referred as 'mode 1' in Phillips et al. (2018), which concerns the accretion of small particles by more massive raindrops, while for snow-raindrop the 'mode 2' formulation is applied. Mode 1 can generate both tiny and big fragments; the former are added to the cloud ice category, while the latter is considered snow. The new tiny fragments are assumed to have a fixed diameter of 10^{-5} m (Phillips et al. 2018) and a constant ice density of 500 kg m^{-3} (which is the default cloud ice density in the MG2 scheme), while the rest of the colliding rain mass is transferred to snow. Freezing probability in this mode is set to unity and zero, at temperatures below -6^{o}C and above -3^{o}C, respectively, while it takes intermediate values at temperatures between -6^{o}C and -3^{o}. Similarly, the shattering probability is a function of raindrop size, set to 0 and 1 at sizes smaller than 50 μm and larger than 60 μm, respectively. Mode 2 can only generate tiny fragments. Tiny fragments are added to the cloud ice category, while big fragments are treated as snow.

Deshmukh et al. (2022) recently developed an empirical formulation for sublimation

break-up of graupel and dendritic snow, in which the total number of the ejected fagments (N) is proportional to the square root of the sublimated mass (M), $N = K \cdot M^{0.57}$, where K is a function of size (diameter) and relative humidity with respect to ice. Since graupel is not accounted in the MG2 scheme, we apply this parameterization to sublimating snow and cloud ice, as long as the diameter for the latter exceeds 200 μm (note that the cloud-ice to snow autoconversion diameter is set to 500 μm in NorESM2). Sublimating cloud ice and snow mass is calculated by the default MG2 scheme. Moreover, since Deshmukh et al. (2022) parameterization is developed based on the observation of dendritic particles, we only allow for sublimation break-up to activate between -10^{o}C and -20^{o}C, where such ice habits are more likely to occur in reality (Bailey and Hallet 2009). All new fragments are added to the cloud-ice category. Sublimation break-up of graupel, which is expected to occur at all temperatures (Deshmukh et al. 2022), is not accounted in the model, since graupel is not treated in MG2.

Finally, while PIP and SIP are significant ice-crystal sources, aggregation is a critical sink that can substantially decrease the cloud-ice number, while its parameterization is also a source of uncertainty in atmospheric models (Karrer et al. 2021). MG2 scheme accounts for aggregation through cloud ice-snow and snow-snow collisions. The accretion of cloud ice by snow follows the "continuous collection" approach as described in Rutledge and Hobbs (1983), while snow-snow aggregation follows Passarelli (1978). Aggregation efficiency (E_{ii}) between ice particles is considered the product of collision efficiency and sticking efficiency, with the latter depending on collisional kinetic energy and size (Phillips et al. 2015). However, a very simplified approach for E_{ii} is usually found in climate models; in CAM6-Oslo this parameter is set constant and t to 0.5 (while it was 0.1 in the previous model version).

c. Sensitivity simulations

In this study, we examine the sensitivity of Arctic clouds to three main processes that determine cloud ice number: PIP, SIP and ice aggregation. At this point, it is worth noting that a bug has been recently identified in MG2 (Shaw et al. 2021), which limits ice formation in mixed-phase clouds. This is due to an upper limit (n_{imax}) imposed for the ICNCs, which is equal to the INP number. Neither heterogeneous freezing processes nor SIP contribute to this INP limit, preventing them from producing new ice crystals (Shaw et al. 2021). In all our simulations we remove this n_{imax} limit, allowing PIP and SIP to evolve prognostically in the stratocumulus clouds. Our investigations on PIP effects include the use of either the prognostic or the diagnostic treatment for the freezing processes (see section 2*b*). Simulations

that employ the Hoose and Möhler (2012) parameterization include the abbreviation 'CNT' in their name, while the ones that are run with diagnostic descriptions (Meyers et al. 1992; Bigg 1953; Young et al. 1974) include the prefix 'MBY' (Table 1). The CNT simulation is also referred as 'control' simulation in the text, as this is the model set-up utilized in CMIP6.

Sensitivity to SIP descriptions is examined by (a) either accounting for the standard SIP treatment in CAM6-Oslo which includes only the HM process after cloud droplet - snow collisions or (b) activating all the additional mechanisms, described in section 2*b*, simultaneously. Moreover, the performance of SIP processes like BR, which are a function of collisional kinetic energy, can be sensitive to different implementation methods. In this study we examine the performance of bulk vs hybrid-bin descriptions of SIP. Our bulk implementations follow the methodology of Sotiropoulou et al. (2020; 2021a,b) and Georgakaki et al. (2022) for BR and DSH, respectively. In their studies, the characteristic diameters and number-weighted velocities for each hydrometeor are used as input parameters for Phillips et al. (2017a) and (2018) schemes, while the standard MG2 formulations for accretion/aggregation rates are used to estimate the collisions that lead to SIP.

However, the MG2 scheme does not account for the accretion of cloud ice on raindrops. To estimate the number and mass collision tendencies for these interactions, we further implement the formulation proposed by Reisner et al. (1998), which is also utilized in the Morrison et al. (2005) scheme. Furthermore, to account for underestimations in collisional kinetic energy when the terminal velocity of the two colliding particles is similar ($u_1 \approx u_2$), we adapt the corrections in the mass- or number-weighted difference in terminal velocity (Δu_{12}) proposed by Mizuno (1990) and Reisner et al. (1998) in the bulk SIP implementations. When snowflakes collide with each other, it is assumed that 0.1% of the colliding mass is transferred to the generated fragments (Phillips et al. 2017a). The same assumption is applied for mode 2 of the drop-shattering process, thus only 0.1% of the colliding mass is transferred to the tiny fragments (Phillips et al. 2018). A detailed description of the implementation method can be found in Sotiropoulou et al. (2021a) and Georgakaki et al. (2022).

On the contrary, Zhao et al. (2021) used an emulated bin approach for these two mechanisms, that better accounts for the impact of the size spectra variability. In their framework, the collision rates are calculated for each bin as $E_c\, \delta N_1\, \delta N_2\, \pi\, (r_1+r_2)^2\, |\, u_1-u_2|$, where E_c is the collision efficiency, and δN_1 and δN_2 are the number concentrations in the two bins with particle radiuses r_1 and r_2, respectively. Similarly, to the bulk approach described above, the number of generated fragments per collision is estimated following Phillips et al.

296 (2017, 2018). Each new fragment produced by these two processes is assumed to have a 10-
297 μm size (Phillips et al. 2018). Sensitivity simulations that account for all SIP mechanisms
298 include the abbreviation 'SIP' in their name (Table I), while if an emulated bin framework is
299 used instead of a bulk description, this suffix is modified to 'SIPBN'. Note that the emulated
300 bin framework is only tested for BR and DSH; the adapted bin diameter ranges follow Zhao et
301 a. (2020), being from 0.1 to 6.5 mm for raindrops (24 bins) and 0.1 to 50 mm for snow and
302 cloud ice particles (35 bins). Each bin diameter (D) is estimated following $D_{k+1}=CD_k$
303 with C=1.2, discretizing the raindrop and ice particle size range in 24 and 35 bins
304 respectively. A bulk approach is used for HM and sublimation break-up in all simulations.
305 Previous applications of these parameterizations in Arctic conditions (Sotiropoulou et
306 al. 2020; Zhao et al. 2022) has shown that BR is the dominant SIP mechanism. However,
307 Sotiropoulou et al. (2021b) showed that the Phillips et al. (2017a) parameterization is largely
308 sensitive to the sublimation factor (ψ) – a correction factor for ice enhancement due to
309 sublimation included in the BR formulation (see Appendix A). This factor was induced to
310 account for the fact that the field data (Vardiman, 1978) used to constrain the number of
311 fragments generated by this the prescribed ψ in Phillips et al. (2017a) study is overestimated,
312 leading to underestimation of the BR efficiency. For this reason we perform two more
313 sensitivity simulations, with both prognostic and diagnostic PIP, with this factor removed
314 from the BR formulation. These experiments include the suffix 'SIPBNψ' in their name, as
315 they are combined with the more advanced emulated bin framework
316 Finally, ice aggregation is another process that has a significant impact on ICNCs but is
317 highly-tuned in climate models. Generally observations from mid-latitudes indicate the
318 presence of two temperature zones that promote aggregation: one around -15°C (Barret et al.
319 2019) associated with enhanced dendritic growth that facilitates the interlocking of the ice
320 crystal branches (Connoly et al. 2012), and a second one close to the melting layer (Lamb and
321 Verlinde 2011), caused by the increased sticking efficiency of melting snowflakes. However,
322 an analysis of recent dual-wavelength radar observations of shallow clouds from Ny-Ålesund
323 suggest that enhanced aggregation occurs between -10^{o}C and -15^{o}C (Chellini et al. 2022),
324 while no evidence of this process is found at higher temperatures. To adjust the aggregation
325 efficiency to these new findings we perform simulations with modified E_{ii}. While in the
326 standard scheme the aggregation efficiency remains constant to 0.5 throughout the whole
327 temperature range, in our sensitivity simulations with the suffix 'AGG' this high value is only
328 sustained between -10^{o}C and -15^{o}C. At colder temperatures E_{ii} is set to 0.1, while at warmer

temperatures aggregation is deactivated (E_{ii}=0). A description of all the performed sensitivity tests and the different combinations of PIP, SIP and aggregation treatments is given in Table 1.

TABLE 1: Description of the sensitivity simulations

	Primary Ice Production	Secondary Ice Production	Aggregation
CNT (CONTROL)	prognostic (CNT)	HM (cloud droplet-snow)	constant E_{ii}
MBY	diagnostic (Meyers et al., Bigg , Young)	HM (cloud droplet-snow)	constant E_{ii}
CNT_AGG	prognostic (CNT)	HM (cloud droplet-snow)	variable E_{ii}
MBY_AGG	diagnostic (Meyers et al., Bigg, Young)	HM (cloud droplet-snow)	variable E_{ii}
CNT_SIP	prognostic (CNT)	HM (cloud droplet/rain-snow), bulk BR, bulk DS, SUBBR	constant E_{ii}
MBY_SIP	diagnostic (Meyers et al., Bigg, Young)	HM (cloud droplet/rain-snow), bulk BR, bulk DS, SUBBR	constant E_{ii}
CNT_SIPBN	prognostic (CNT)	HM (cloud droplet/rain-snow), bin BR, bin DS, SUBBR	constant E_{ii}
MBY_SIPBN	diagnostic (Meyers et al., Bigg, Young)	HM (cloud droplet/rain-snow), bin BR, bin DS, SUBBR	constant E_{ii}
CNT_SIPBNψ	prognostic (CNT)	HM (cloud droplet/rain-snow), bin BR (ψ=1), bin DS, SUBBR	variable E_{ii}
MBY_SIPBNψ	diagnostic (Meyers et al., Bigg, Young)	HM (cloud droplet/rain-snow), bin BR (ψ=1), bin DS, SUBBR	variable E_{ii}
CNT_SIPBN_AGG	prognostic (CNT)	HM (cloud droplet/rain-snow), bin BR, bin DS, SUBBR	variable E_{ii}
MBY_SIPBN_AGG	diagnostic (Meyers et al., Bigg, Young)	HM (cloud droplet/rain-snow), bin BR, bin DS, SUBBR	variable E_{ii}
CNT_SIPBNψ_AGG	prognostic (CNT)	HM (cloud droplet/rain-snow), bin BR (ψ=1), bin DS, SUBBR	variable E_{ii}
MBY_SIPBNψ_AGG	diagnostic (Meyers et al., Bigg, Young)	HM (cloud droplet/rain-snow), bin BR (ψ=1), bin DS, SUBBR	variable E_{ii}

3. Results

a. Ny-Ålesund site

1) Cloud properties

In this section we focus on the evaluation of the simulated cloud macrophysical properties against remote-sensing surface observations collected at Ny-Ålesund (see section 2*a*). An evaluation of the modeled thermodynamic conditions is presented in Figs. S1 and S2 in the Supporting Information. NorESM2 is in reasonably good agreement with temperature (Fig. S1) and IWV (Fig. S2) measurements, although somewhat colder conditions are often found in the model within the lowest first kilometer of the atmosphere (Fig. S1).

Instantaneous modeled ICNC and IWC values derived at 3-hour time resolution are used in Fig. 1, which presents the median estimates as a function of temperature. ICNCs are constructed from the in-cloud cloud ice number and the in-precipitation snow number, predicted by the model. Similarly, modeled IWC is constructed from the respective in-cloud cloud ice and in-precipitation snow mass mixing ratios. IWC retrievals are averaged over a ±10-minute window around the model output timesteps and within ±20 meters around the model vertical levels, while ICNC measurements are not available at this site. Measurement uncertainty is also plotted in Fig. 1b.

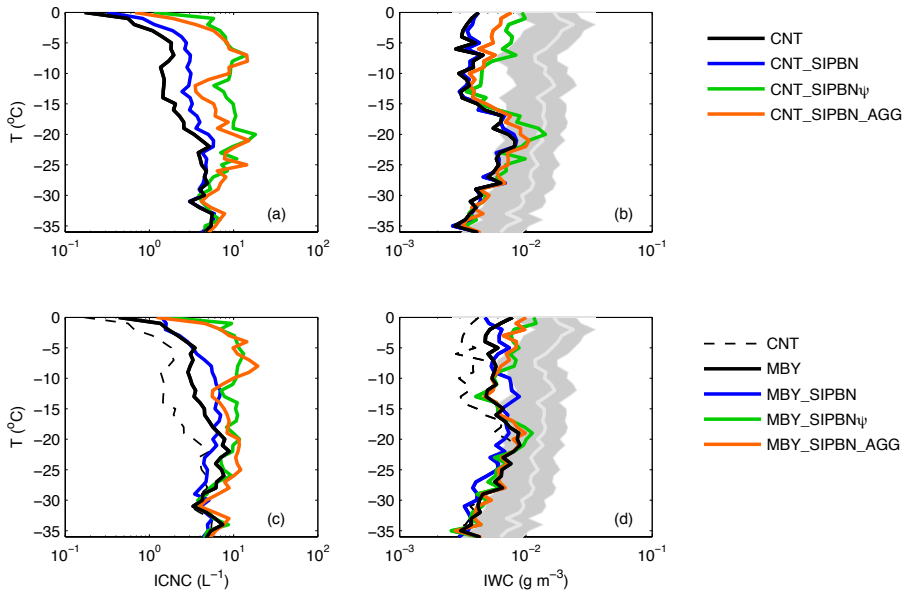

FIG 1. (a, c) Ice crystal number concentration (ICNC) and (b, d) ice water content (IWC) as a function of temperature. Grey shading (line) indicate the uncertainty range (50%) in the measured values. Results are derived from the Ny-Ålesund site (grid-point) for the period June 2016- May 2018. The observed IWC values are averaged over a ±10-minute window around the model output timesteps and within ±20 meters round the model vertical levels.

The aerosol-aware CNT (control) simulation produces median ICNC concentrations round 1.5 L^{-1} within the -5°C to -15°C temperature range (Fig. 1a), which results in a median IWC that is on average five times lower than the observed (Fig. 1b). The IWC discrepancies between CNT and observations are reduced below -15°C: the median IWC is only two times

lower than the observed median at these cold temperatures and lays very close to the uncertainty range. CNT_SIP does not result in any ice enhancement; for this reason it is shown in the Supplementary Information (Figure S3). CNT_SIPBN results in a weak ICNC enhancement within the temperature range that is favorable for SIP (Fig. 1a), compared to CNT, with hardly any impact on median IWC (Fig. 1b). CNT_AGG produces similar results to CNT_SIPBN (Fig. S3), thus activating SIP or decreasing ice aggregation has a similar effect on ICNCs. CNT_SIPBNψ and CNT_SIPBN_AGG produce similar ICNC enhancements, resulting in 5-15 times larger median values (Fig. 1a) at the relatively high (>-15^{o}C) temperatures compared to CNT. Median ICNC values are close to 10 L^{-1} in these two simulations (Fig. 1a), which are in agreement with recent SIP observations from Arctic clouds at Ny-Alesund (Pasquier et al. 2022). Median IWC is 2-3 times larger in CNT_SIPBNψ and CNT_SIPBN_AGG at temperatures above -15^{o}C, compared to CNT, in closer agreement with observations (Fig. 1b). CNT_SIPBNψ_AGG, which includes both the modified ψ factor and decreased aggregation results in reasonable agreement with the observed IWC (Fig. S3b), however median ICNCs exceed 100 L^{-1} (Fig. S3a). Such median values are extreme and have not been observed in the Arctic. Since this set-up results in unrealistic microphysical properties, it is excluded from the rest of the analysis.

The MBY simulation (Fig. 1c) produces about 2-2.5 times higher median ICNCs than CNT at temperatures above -15^{o}C, which increases median IWC values by 50-80% (Fig. 1d), in slightly better agreement with observations. No improvement in IWC is found at colder temperatures with the diagnostic PIP treatment. MBY_SIPBN results in negligible differentiations compared to the MBY simulation that do not affect the ice macrophysical state of the modeled clouds (Fig. 1d). The same applies for MBY_SIP and MBY_AGG, shown in the supplementary information (Fig. S3). Similarly to CNT_SIPBNψ and CNT_SIPBN_AGG, MBY_SIPBNψ and MBY_SIPBN_AGG produce median ICNCs close to 10 L^{-1}, which are realistic for Arctic SIP conditions observed at Ny-Alesund (Pasquier et al. 2022); these set-ups in somewhat improved IWC at temperatures above -15^{o}C. Despite the improved median IWC in MBY_SIPBNψ_AGG (Fig. S3d), this simulation produces unrealistically high median ICNCs (> 100 L^{-1}), similar to CNT_SIPBNψ_AGG (Fig. S3a,c). and thus this simulation is also excluded from the following analysis.

It is worth noting that CNT_SIPBN_AGG (MBY_SIPBN_AGG) is substantially more efficient in ICNC enhancement than CNT_SIPBN (MBY_SIPBN) and CNT_AGG (MBY_AGG), which are more similar (Fig. S3). This indicates an important interplay

between SIP and decreased ice aggregation, when combined together. An overestimated aggregation rate can substantially limit ice multiplication, as the new fragments will rapidly aggregate and form precipitation-sized particles that will lead to IWC depletion through sedimentation (Fig. S4). It is worth noting that the worst CNT_SIPBN_AGG and MBY_SIPBN_AGG performance is found at temperatures between -10°C and -15°C, where the default aggregation efficiency remains unaffected (see section 2*c*). This suggests that constraining ice aggregation is critical for the representation of Arctic cloud properties, particularly in conditions that favor SIP.

ICNC measurements were not conducted at Ny-Ålesund in 2016-2018, thus the ICNC profiles presented in Fig. 1 cannot be evaluated against observations. Only measured cloud particle concentrations over a limited size range (5-50 μm) collected with a CVI are available (see section 2*a*). These are shown in Fig. 2 along with the modeled in-cloud droplet and cloud ice size spectra that include the measured size range. Size spectra of larger particles, rain and snow (in-precipitation values), are also shown in the same figure to give a complete overview of the microphysical differences between the different simulations.

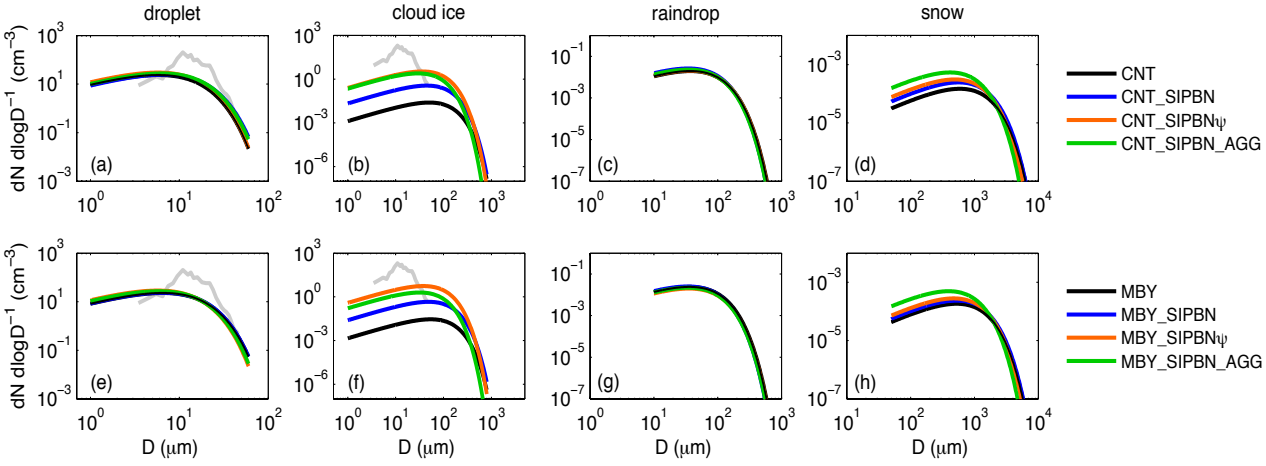

FIG 2. (a, e) droplet, (b, f) cloud ice, (c, g) raindrop and (d, h) snow size distributions for the different model sensitivity simulations. The first (second) row of panels presents simulations conducted with prognostic (diagnostic) PIP. Grey lines in panels (a, e) and (b, f) represent the observed spectrum derived from CVI for the size range 5-50 μm. All data span the period June 2015 - February 2018, as CVI measurements were not collected beyond this date.

All model simulations underestimate the hydrometeor concentrations measured by the CVI at a size between 10-30 μm. Differentiations in liquid hydrometeors among the simulations are small (Fig. 2a,c,e,g), while more pronounced differences among the simulations are found in the cloud ice particle spectra. Increasing ice production (Fig. 1)

substantially enhances the smaller particles (Fig. 2b, f) in CNT_SIPBNψ, CNT_SIPBN_AGG, MBY_SIPBNψ and MBY_SIPBN_AGG simulations. This improves the agreement with observations particularly within the 10-30 μm size range, where CNT and MBY produce the largest cloud-ice underestimations. CNT_AGG (MBY_AGG) and CNT_SIP (MBY_AGG) are not included in Fig. 2, as they produce very similar spectra to CNT (MBY) and CNT_SIPBN (MBY_SIPBN), respectively. Yet the large concentrations of such small particles measured by the CVI are not produced by any model set-up. Another fact that may affect the model's performance is that it does not account for blowing snow, a mechanism that is commonly observed in mountainous regions and is known to provide the clouds with small ice particles raised from the surface during windy conditions *(Gossart et al. 2017)*. Distinct differences are also found in the snow size spectra (Fig. 2d, h) , with the most pronounced shifts towards smaller snowflakes produced by simulations with reduced aggregation. This is however expected as aggregation directly augments the mass of snow particles either through self-collection or collection of cloud ice.

Apart from the CVI observations collected on mount Zeppelin, insights into the particle sizes can be obtained from the radar-retrieved r_{ieff}. However, this dataset is associated with large uncertainties (see section 2*a*). The retrievals result in a median r_{ieff} of 44 μm for measurements collected above -20^{o}C. This value is 79.8 μm for CNT and 79.3 μm for MBY and somewhat decreases in simulation with increased ice production. Among the simulations that utilize CNT PIP scheme, shown in Figs 1 and 2, CNT_SIPBN_AGG produces the median r_{ieff} closest to the observed (67.8 μm), while among the simulations with the diagnostic PIP, MBY_SIPBNψ produces the smaller radii (64.5 μm). However, the differences in the modeled r_{ieff} do not exceed ~15 μm between the different model set-ups, which is substantially smaller than the uncertainty in the r_{ieff} retrieval, indicating these measurements cannot be used for a robust microphysical evaluation.

LWP measurements exhibit considerable variability throughout the year; for this seasonal LWP statistics are presented in Table 2. Moreover, as LWP distribution appears highly skewed, especially during winter and spring, both mean and median values are included in the Table. Observational statistics are also included in Table 2, derived from LWP measurements interpolated at the model timesteps. Modeled LWP is constructed from the in-cloud droplet mixing ratios.

Simulations with CNT produce generally more LWP than those that utilize the diagnostic PIP scheme. All simulations substantially overestimate LWP in summer.

458 Increasing ice production results in decreasing in-cloud LWPs, in better agreement with
459 observations. MBY_SIPBNψ produce the lowest LWP values in summer, however these
460 remain substantially overestimated compared to the observed. CNT simulation produces a
461 larger LWP overestimation in autumn compared to MBY, as the latter deviates ~38 g m^{-2}
462 (~16 g m^{-2}) from the mean (median) observed value. Increasing ice production results in
463 improved liquid statistics, with CNT_SIPBNψ producing in-cloud LWPs closer to the
464 observed than any other simulation that employs a prognostic PIP scheme. MBY_SIPBN,
465 MBY_SIPBNψ and MBY_SIPBN_AGG produce mean and median in-cloud LWP values
466 closer to the observed than MBY.

467 CNT overestimates LWP in winter, while MBY produces in-cloud values very similar to
468 the observed. As a result, enhancement in ice production for simulations that treat PIP through
469 CNT improves agreement with observational statistics. In particular, CNT_SIPBNψ set-up
470 produces the most realistic mean value, while CNT_SIPBNψ gives a better representation of
471 the median winter LWP. In contrast, MBY_SIPBN_AGG and MBY_SIPBNψ produce
472 underestimated LWP compared to the MBY and MBY_SIP, leading to larger deviations from
473 the observations. Finally, model performance in spring for LWP is similar to winter:
474 simulations with CNT somewhat overestimate LWP (albeit the deviations are less pronounced
475 than for summer and autumn seasons), while increasing ice production improves agreement
476 with measurements. On contrary the set-ups that utilize the diagnostic PIP scheme produce
477 more realistic LWP, with MBY and MBY_SIP being closer to the observed values.
478
479 **TABLE 2:** in-cloud Liquid Water Path (LWP, g m^{-2}) for observations and sensitivity
480 simulations, segregated into mea/median seasonal values.

	summer	**autumn**	**winter**	**spring**
Observations	**79.8/ 39.6**	**76.9/ 23.6**	**34.1/ 2.7**	**38.1/ 2.9**
CNT (CONTROL)	167.2/ 132.0	147.8/ 87.3	72.3/ 7.9	76.7/ 13.1
CNT_SIPBN	164.1/ 127.3	139.2/ 74.4	62.3/ 4.3	71.0/ 8.3
CNT_SIPBNψ	160.1/ 121.7	114.5/ 36.0	29.4/ 10^{-5}	50.1/ 4.4
CNT_SIPBN_AGG	162.2/ 122.1	145.9/ 95.5	56.7/ 3.6	62.2/ 8.0
MBY	145.3/ 112.0	115.2/ 39.9	36.6/ 2.3	41.9/ 5.1
MBY _SIPBN	145.7/ 112.1	102.2/ 23.1	34.6/ 2.3	40.9/ 4.7
MBY_SIPBNψ	145.2/ 103.7	102.7/ 18.0	20.8/ 10^{-5}	27.2/ 2.0

MBY_SIPBN_AGG	145.9/ 106.8	104.8/ 25.4	29.5/0.3	32.7/ 4.2

2) Microphysical processes

To better understand the interactions between the underlying microphysical processes that drive the macrophysical differences between the different sensitivity simulations, vertical profiles of mean PIP, SIP, WBF and riming tendencies are plotted in Fig. 3. The ice multiplication tendencies of the individual SIP mechanisms are shown in Fig. 4. Interestingly, when a diagnostic PIP treatment is applied (Fig. 3e), PIP rates generally decrease with increasing ice production through modifications in SIP or aggregation, a behavior that is not found in simulations with CNT (Fig. 3a). An analysis of the changes in thermodynamic profiles between the simulations (Fig. S5a, c) indicate warmer temperatures with increasing ice production, especially at heights above 1 km, while the specific humidity response is more variable (Fig. S5b, d); since the diagnostic PIP parameterizations are solely dependent on the thermodynamic conditions, these temperature variations can explain to a large extent the variable PIP rates in Fig. 3e. In Fig. 3a substantial differences in PIP are mainly found in CNT_SIPBNψ; these differences seem to follow changes in specific humidity profiles (Fig. S5b, d) suggesting that the prognostic PIP treatment is mostly affected by variations in supersaturation.

SIP rates in CNT_SIP and MBY_SIP are very similar to CNT and MBY (Fig. 4b, f). This is in agreement with the findings of Fig. S1, which reveal that the bulk implementations of BR and DSH hardly result in any ice multiplication. This result is further confirmed by Fig. 4 which shows that BR and DSH tendencies are orders of magnitude smaller than those of HM. Another interesting finding is that including rain-snow collisions in the HM description in the CNT_SIP and MBY_SIP simulations does not enhance the efficiency of this process compared to CNT and MBY that account only for cloud drop-snow collisions (Fig. 4a, e), as the precipitation particle concentrations are generally limited (Fig. 2c,d,g,h). Furthermore, sublimation breakup activates in the lowest five atmospheric kilometers but remains extremely weak through the whole layer (Fig. 4d, h).

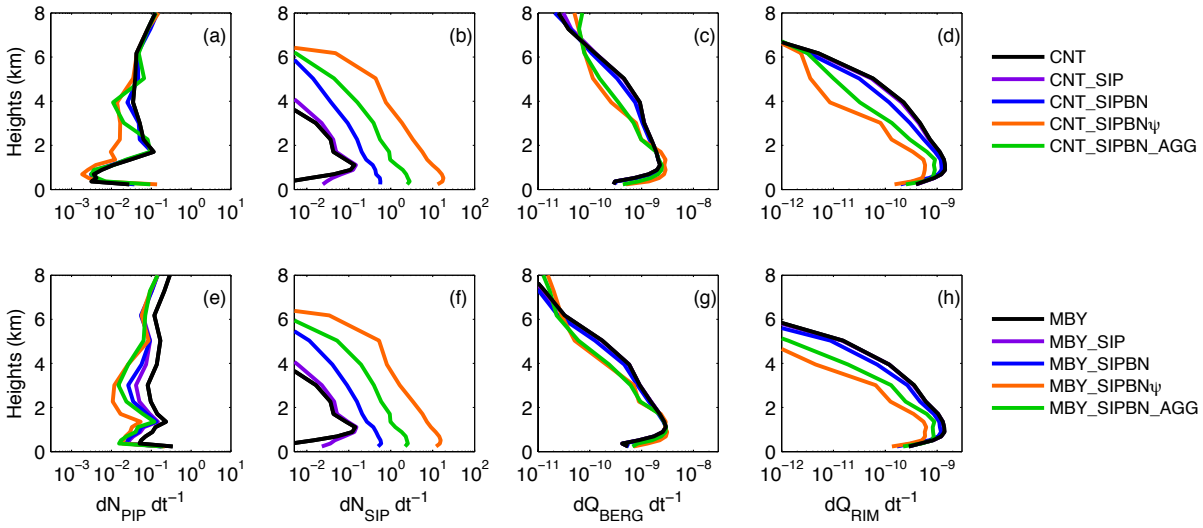

FIG 3. Mean vertical profiles of number concentration tendencies (kg^{-1} s^{-1}) due to (a, e) PIP (dN_{PIP} dt^{-1}) and (b, f) SIP (dN_{SIP} dt^{-1}), (c, g), and mass concentration tendencies (kg kg^{-1} s^{-1}) due to WBF (dQ_{BERG} dt^{-1}) and (d, h) riming (dQ_{RIM} dt^{-1}) for the different model sensitivity simulations. The WBF rate is the sum of the individual rates for cloud ice and snow particles, while riming is the sum of cloud droplet and rain accretion on snow. The first (second) row of panels presents simulations conducted with prognostic (diagnostic) PIP.

Utilizing an emulated bin framework for BR and DSH enhances SIP rates by on average a factor of ~5 in the lowest 4 atmospheric kilometers, compared to the simulations that adapt bulk frameworks (Fig. 3b, f). SIP also becomes prominent at higher altitudes (> 4 km), where bulk parameterizations do not produce any ice multiplication. Figure 4 indicates that the SIP is mainly due to the BR process. Although the emulated bin framework enhances DSH efficiency, the DSH rates remain substantially lower than those that correspond to the BR mechanism. Decreasing aggregation in CNT_SIPBN_AGG and MBY_SIPBN_AGG increases SIP efficiency by on average a factor of 5 (Fig. 3b, f), compared to CNT_SIPBN and MBY_SIPBN simulations, mainly through the enhancement of the BR process (Fig. 4b, f). Interestingly, the largest sensitivity of SIP is found in the treatment of the sublimation correction factor ψ in BR description. The simulation with ψ=1 (Table 1), that does not account for this correction results in BR rates enhanced by 1-1.5 orders of magnitude (Fig. 4b,f), which highlights the importance of constraining this parameter for an accurate BR representation. It is worth noting that increasing BR efficiency is associated with decreasing HM rates (Fig. 4). This is due to the fact that increasing SIP results in smaller ice particle sizes that are less likely to rime and initiate HM. The impact of SIP on riming and the WBF efficiency will be discussed below.

The simulations with a modified ψ factor or aggregation efficiency are characterized by an enhanced (reduced) WBF efficiency in the low-level (mid-level) clouds (Fig. 3c, g) compared to the rest of the simulations that produce significantly less ice content (Fig. 1). These simulations are also characterized by decreased riming efficiency throughout the whole troposphere (Fig. 3d, h). This is likely due to the shift of the frozen hydrometeor spectra to smaller particle sizes (Fig. 2) that are less efficient in depositional growth and liquid accretion. The more active WBF mechanism in the low-level clouds is likely responsible for the reduced in-cloud LWPs (Table 2).

Our findings indicate that the inclusion of missing SIP mechanisms in NorESM2 can improve the macrophysical representation of Arctic mixed-phase clouds, but this requires the use of an emulated bin framework for BR and DSH, which is computationally about two times more demanding than the bulk descriptions of SIP. Modifications in the HM description, with the inclusion of rain-snow interactions, did not enhance the efficiency of this process in the examined conditions, suggesting that these modifications are redundant. BR appears to be the dominant SIP mechanism, however its efficiency is very sensitive to the treatment of the poorly constrained parameter ψ. DSH and SUBR processes are substantially weaker in the examined conditions. DSH is likely not favored due to lack of relatively large drops to initiate the process (Fig. 2c, g), while SUBBR is likely limited by the high relative humidity conditions that generally dominate in the Arctic.

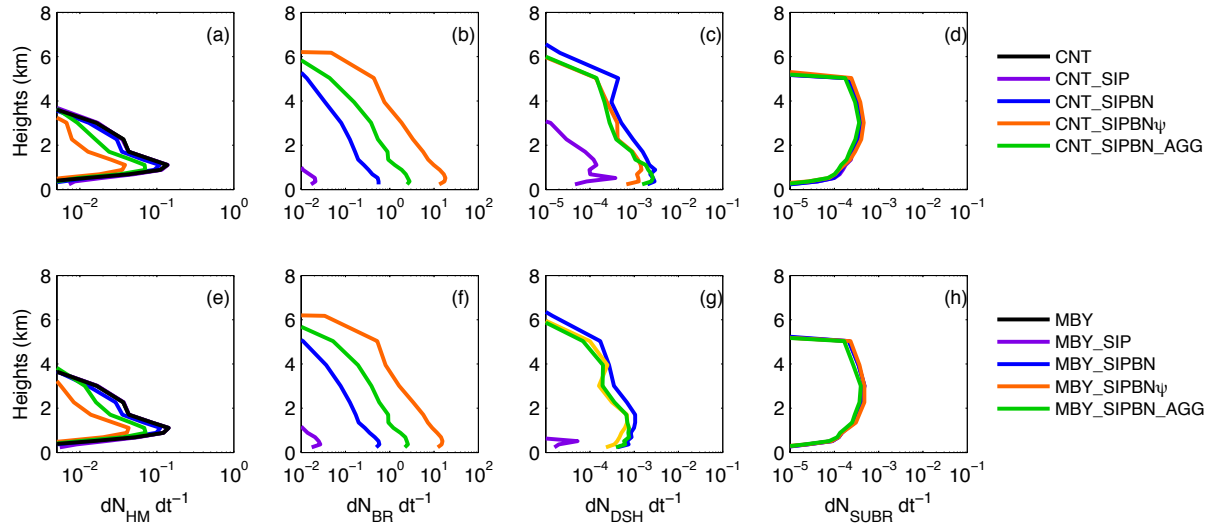

FIG 4. Mean vertical profiles of number concentration tendencies (kg^{-1} s^{-1}) due to SIP from the (a, d) HM, (b, f) BR and (c, f) DSH and (d, h) SUBBR for the different model sensitivity simulations. The first (second) row of panels presents simulations conducted with prognostic (diagnostic) PIP.

b. Arctic region

In this section, the performed simulations are evaluated against satellite observations averaged over the whole Arctic region (>66^{o}N). In Table 3 the simulated net cloud radiative effects (CRE) at the Top Of the Atmosphere (TOA) are compared to EBAF v4.1 products. Differences in the net surface cloud radiative effect are found less significant and thus are not shown. Furthermore, in Table 4 the modeled and observed total cloud cover is presented; the latter is represented by the GOCCP product. Two values are shown for the different simulations: (a) the COSP output which is suitable for comparison with the satellite observations and (b) the direct model outputs, which control radiation (Table 4).

Net CRE at TOA is negative in summer and spring, as shortwave effects dominate, while during autumn-winter, when incoming solar radiation is weaker, the dominance of the longwave components result in positive values. The simulations that utilize the CNT PIP scheme produce enhanced warming (cooling) at TOA autumn-spring (summer) than the simulations with diagnostic PIP parameterizations, resulting in slightly better (worse) agreement with EBAF observations. CNT overestimates cloud radiative cooling at TOA in summer by 5.3 W m^{-2} and overestimates cloud induced warming during the rest of the seasons, with the largest deviations from EBAF observations found in winter (4.6 W m^{-2}). CNT_SIPBN produces very similar results to CNT, while the two simulations with the enhanced ice production produce larger net longwave effects (Table S1), shifting the net CRE towards warmer values. This improves the representation of the net cloud radiative effect during most of the year, with the largest improvements found in winter for CNT_SIPBN_AGG (~3 W m^{-2}). Differences in shortwave CRE at TOA among the simulations are generally smaller, never exceeding 1.5 W m^{-2} (Table S2). The response of the simulations with diagnostic PIP to increasing ice production is similar to those that employ CNT, but weaker in magnitude. As a result, the differences between MBY and MBY_SIPBN_AGG or MBY_SIPBNψ are generally small (<1.5 W m^{-2}). The most pronounced improvement in net CRE is found in simulation MBY_SIPBNψ for the summer season, however this is due to compensating errors between the shortwave and longwave components (Tables S1,S2).

Table 3: Cloud Radiative Forcing at TOA

	summer	**autumn**	**winter**	**spring**

EBAF observations	**-44.6**	**6.6**	**12.4**	**-7.1**
CNT (CONTROL)	-49.9	5.3	7.8	-1.9
CNT_SIPBN	-49.1	5.3	7.9	-1.8
CNT_SIPBN_AGG	-48.5	7.5	10.8	-1.6
CNT_SIPBNψ	-47.6	6.2	8.6	-1.2
MBY	-46.7	4.6	7.7	-0.8
MBY _SIPBN	-46.1	4.7	7.8	-0.7
MBY_SIPBN_AGG	-46.5	4.8	8.4	-0.8
MBY_SIPBNψ	-45.3	4.8	8.4	-0.5

590

591 COSP total cloud cover for CNT and MBY simulations is in good agreement with EBAF
592 observations in summer (Table 4), but underestimates cloud cover during the rest of the
593 seasons, especially in winter and spring. Increasing ice production result in somewhat
594 increased total cloud cover: the difference between CNT (MBY) and the simulation that
595 produces the largest ice content, CNT_SIPBNψ (MBY_SIPBNψ), is about 1-1.5% (1-4%).
596 Increasing COSP cloud cover is mainly caused by increased high cloud cover (Tables S4);
597 COSP mid-level cloud cover exhibits little sensitivity to variations in ice treatment (not
598 shown), while COSP low-level cloud cover decreases with increasing ice production (Table
599 S3). However, this behaviour is not found in the direct model output, in which both total and
600 low-level cloud cover increase in the simulations with enhanced ice content (Table S3). A
601 possible explanation for this discrepancy is that as the enhanced ice production results in
602 optically-thinner layers, the fraction of the very thin clouds that do not pass the detection
603 thresholds applied in the COSP simulator increases. The direct model outputs however are
604 generally compatible with changes in CRE_{LW} at TOA (Table S1), as increasing cloud cover
605 reduces outgoing thermal radiation, resulting in a warming effect.

606

607 **Table 4:** TOA COSP /model total Cloud cover

	summer	**autumn**	**winter**	**spring**
EBAF observations	**80.7**	**79.6**	**63.3**	**70.3**
CNT (CONTROL)	81.5/ 85.0	75.6/ 85.6	57.8/ 78.0	55.4/ 74.7
CNT_SIPBN	81.5/ 85.0	75.2/ 85.5	57.6/ 78.0	54.8/ 74.6
CNT_SIPBN_AGG	82.3/ 85.7	75.7/ 86.3	57.6/ 79.0	54.7/ 75.5

CNT_SIPBNψ	82.6/ 86.1	75.7/ 86.8	57.0/ 79.2	53.9/ 75.5
MBY	79.7/ 83.8	69.8/ 83.7	50.7/ 76.7	46.4/ 71.5
MBY _SIPBN	79.7/ 83.8	69.7/ 83.9	60.0/ 76.9	46.2/ 71.5
MBY_SIP_AGG	80.4/ 84.5	70.3/ 84.6	52.2/ 78.1	47.0/ 72.4
MBY_SIPBNψ	80.5/ 84.8	70.6/ 85.0	54.0/ 78.3	46.8/ 72.3

4. Summary

In this study, we examine the sensitivity of Arctic cloud properties to the representation of ice microphysical processes in NorESM2. The primary target is to quantify the impact of PIP and SIP parameterizations on the cloud macrophysical structure and radiative effects. Sensitivity simulations with PIP are performed with two different primary ice treatments: (a) a prognostic CNT scheme that explicitly predicts ice formation from cloud-aerosol interactions and (b) diagnostic temperature-dependent parameterizations for all the heterogeneous freezing processes. The standard version of NorESM2 accounts only for the HM process through droplet-snow collisions. The sensitivity to SIP is examined by implementing additional SIP mechanisms, namely the BR, DSH and SUBBR mechanisms. Furthermore, the HM description is modified to account for rain-snow collisions, following Morrison et al. (2005).

The interactions of PIP and SIP with ice aggregation are also a subject of the present study. The standard parameterization of this process in NorESM2 includes a constant aggregation efficiency (E_{ii}) set to 0.5. To investigate the sensitivity of our results to this parameter, we adapt a variable E_{ii} which is qualitatively constrained by recent dual-wavelength radar measurements of shallow Arctic clouds (Chellini et al. 2022): E_{ii} is set to 0.5 at temperatures between -10^{o}C and -15^{o}C and to 0 (0.1) at temperatures below (above) this range. The model results are evaluated against surface observations from Ny-Ålesund and satellite retrievals over the whole Arctic.

Using CNT instead of diagnostic PIP descriptions results in a worse agreement with IWC observations from Ny-Ålesund at temperatures between -5^{o}C and -15^{o}C, when no other modification in SIP or aggregation is implemented. We speculate that the reason for this behavior is that the NorESM2 CNT parameterization does not account for aerosol types that are efficient INPs at relatively warm temperatures (e.g. biological aerosols). This larger underestimation in ice content is accompanied by substantially overestimated LWP, compared to the observed.

Activating the missing SIP mechanisms enhances ice content, mainly through the BR process. BR efficiency however highly depends on the treatment of the correction factor ψ, which is included in the Phillips et al. (2017a) parameterization to account for the ice enhancement due to sublimation. This is a poorly constrained parameter, while the value assigned by Phillips et al. (2017a) likely results in underestimations of the BR effect. DSH and SUBBR are the two mechanisms with the weakest efficiency in the examined conditions. Moreover, modifications in the HM description to account for rain-snow collisions do not enhance the efficiency of the process. HM and DSH are likely limited by the fact that relatively large raindrops are generally few in the examined conditions. SUBBR is likely not favored due to the high relative humidity conditions that often persist in polar environments.

It is worth noting that the current BR and SUBBR implementations can be affected by the number of frozen hydrometeors that are treated in the cloud scheme and MG2 does not account for graupel particles. While Gettelman et al. (2019) showed that the global climate impact of rimed ice in stratiform clouds is negligible in 100-km scale simulations, their study concerns the standard MG2 scheme that does not account for additional SIP mechanisms. Zhao et al. (2020, 2021) on the other hand showed that including graupel can enhance the efficiency of the BR process in Arctic clouds. Similarly, the SUBBR implementation concerns only the snow particles in our model, which can undergo sublimation break-up only within a limited temperature range (see Section 2c). In contrast, sublimation break-up of graupel can occur at any temperature (Deshmukh et al. 2022). In summary, the fact that graupel category is not treated in NorESM2 suggests that the overall efficiency of both BR and SUBBR mechanisms might be underestimated in our simulations.

Interestingly, SIP efficiency increases substantially with decreasing ice aggregation in our simulations. This is because enhanced SIP results in enhanced ice aggregation when a constant aggregation efficiency is assumed. However, in reality, this might not be necessarily true as enhanced SIP may lead to the prevalence of small ice particles that are not efficient in aggregation or to the reduction of dendritic ice crystal concentrations through break-up; dendrites are the ice habits that are known to be most favorable for aggregation (Karrer et al., 2021; Chellini et al., 2022).

Increasing ice production through changes in SIP and /or aggregation decreases has a direct impact on other microphysical processes, such as riming and WBF efficiency. Specifically simulations with higher ice number are characterized by decreased riming throughout the whole vertical profile. In contrast, WBF exhibits a more variable behaviour: it

is less efficient in mid-level clouds, while in low-level clouds below 1-km WBF can become more effective in these simulations. The net effect of all these microphysical processes on the macrophysical structure of the Arctic clouds at Ny-Alesund site is a reduction in cloud liquid and an enhancement in IWC. This improves the agreement of the simulations that utilize the CNT PIP scheme with the field observations, as CNT is characterized by substantially overestimated LWP. In contrast, SIP enhancement or decreased aggregation results in degraded cloud liquid representation in the simulations with the diagnostic PIP scheme.

Finally, as far as SIP/aggregation impacts on cloudiness over the whole Arctic region are concerned, increasing ice production is found to lead to increased total cloud cover. This is mainly due to the fact that these ice microphysical processes shift the overall cloud ice particle spectra towards smaller sizes, extending the cloud particle lifetime in the atmosphere. The largest increases are observed in the modelled low-level cloud cover; weaker increases are found in the high-cloud cover, while mid-level clouds are hardly impacted. The increased cloudiness, results in improved CRE predictions at TOA especially during the cold months, through improvements mainly in the longwave component. The latter is due to enhanced downward longwave emission, which decreases the negative CRE bias that is produced by the standard NorESM2 model in winter.

Acknowledgements:

This study is supported by the H2020-EU.1.3.- EXCELLENT SCIENCE - Marie-Skłodowska-Curie Actions project SIMPHAC (ID 8985685), the project IC-IRIM project (ID 2018-01760) funded by the Swedish Research Council for Sustainable Development (FORMAS) and the project FORCeS funded from Horizon H2020-EU.3.5.1. (ID 821205). We are grateful to Øyvind Seland for providing the NorESM2 code, to Inger Helen Karset for providing python scripts to convert ERA-I data to a format readable by NorESM2 and to Dirk Jan Leo Olivie for further clarifications regarding the model. We are also grateful to the scientists that collected and processed Ny-Ålesund observations and especially to Dr. Tatiana Nomokonova and Prof. Kerstin Ebell for providing clarifications regarding the datasets. The simulations were enabled by resources provided by the Swedish National Infrastructure for Computing (SNIC) at the National Supercomputer Center (NSC), partially funded by the Swedish Research Council through grant agreement no. 2018-05973.

Data availability statement:

Both surface-based and satellite observations are available online. LWP datasets from Ny-Ålesund for the years 2016, 2017 and 2018 can be found at https://doi.org/10.1594/PANGAEA.902096 (Nomokonova et al. 2019a), https://doi.org/10.1594/PANGAEA.902098 (Nomokonova et al. 2019b) and https://doi.org/10.1594/PANGAEA.902099 (Nomokonova et al. 2019c). IWC and Ri_{eff} data can be found at https://doi.pangaea.de/10.1594/PANGAEA.898556 (Nomokonova et al. 2019d). HATPRO temperature profiles can be downloaded from https://doi.org/10.1594/PANGAEA.902145 (Nomokova et al. 2019e), https://doi.org/10.1594/PANGAEA.902146 (Nomokova et al. 2019f) and https://doi.org/10.1594/PANGAEA.902147 (Nomokova et al. 2019g). Ny-Ålesund IWV measurements for the same years are available at https://doi.org/10.1594/PANGAEA.902140 (Nomokonova et al. 2019h), https://doi.org/10.1594/PANGAEA.902142 (Nomokova et al. 2019i) and https://doi.org/10.1594/PANGAEA.902143 (Nomokova et al. 2019j). CVI measurements are available at https://doi.org/10.17043/zeppelin-cloud-aerosol-1 (Karlsson et al. 2021b). The CERES-EBAF data are retrieved from https://ceres.larc.nasa.gov/data/, while GOCCP dataset can be downloaded from https://climserv.ipsl.polytechnique.fr/cfmip-obs/. ERA-Interim reanalysis products can be accessed through https://www.ecmwf.int/en/forecasts/datasets/reanalysis datasets/era-interim. Model datasets will be deposited to zenodo.org upon acceptance of the manuscript.

Appendix A: Sublimation corrector factor in BR formulation

The Phillips et al. (2017a) parameterization predicts the number of fragments (F_{BR}) generated from mechanical break-up upon collisions of two ice particles using the equation:

$$F_{BR} = \alpha A \left(1 - exp\left\{-\left[\frac{CK_o}{\alpha A}\right]^{\gamma}\right\}\right)$$

where K_o is the collisional kinetic energy, α is the surface area of the smaller ice particle that undergoes fracturing, A represents the number density of the breakable asperities in the region of contact, γ is a function of the particle's rimed fraction and C is the asperity-fragility coefficient, which is a function of a correction term (ψ) for the effects of sublimation based on the field observations by Vardiman (1978). Specifically, for planar ice the assigned values are: $C = 7.08 \times 10^{6}\psi$ and $\psi = 3.5\times10^{-3}$. Thus, a ψ value smaller than unity has a decreasing impact on F_{BR} estimation. Setting ψ=1 in the sensitivity simulations with 'ψ' suffix assumes no impact of sublimation break-up on the Vardiman (1978) data used to constrain the above formulation.

740

741 **References:**

742 Bacon, N. J., B. D. Swanson, M. B. Baker, and E. J. Davis, 1998: Breakup of levitated frost
743 particles. *J. Geophys. Res.*, **103**, 13 763–13 775, doi: 10.1029/98JD01162.
744
745 Bailey, M. P., and J. Hallett, 2009: A comprehensive habit diagram for atmospheric ice
746 crystals: Confirmation from the laboratory, AIRS II, and other field studies. *J. Atmos.*
747 *Sci.*, **66**, 2888–2899, doi:10.1175/2009JAS2883.1.
748
749 Barrett, A. I., C. D. Westbrook, J. C. Nicol, and . H. M Stein, 2019: Rapid ice aggregation
750 process revealed through triple-wavelength Doppler spectrum radar analysis, *Atmos. Chem.*
751 *Phys.*, **19**, 5753–5769, doi:10.5194/acp-19-5753-2019

752 Bigg, E. K.: The supercooling of water, *Proc. Phys. Soc. B*, **66**, 688– 694, 1953.

753 Boucher, O., and Coauthors, 2013: Clouds and aerosols. In *Climate Change 2013: The*
754 *Physical Science Basis. Contribution of Working Group I to the Fifth Assessment Report of*
755 *the Intergovernmental Panel on Climate Change* Stocker, T.F. and Coauthors, Eds.
756 Cambridge University Press, pp. 571-657, doi: 10.1017/CBO9781107415324.016.
757
758 Chepfer, H., S. Bony, D. Winker, G. Cesana, J. L. Dufresne, P. Minnis, C. J. Stubenrauch,
759 and S. Zeng, 2010: The GCM-Oriented CALIPSO Cloud Product (CALIPSO-GOCCP), *J.*
760 *Geophys. Res.*, **115**, D00H16, doi: 0.1029/2009JD012251
761
762 Connolly, P. J., C. Emersic, and P. R. Field, 2012: A laboratory investigation into the
763 aggregation efficiency of small ice crystals, *Atmos. Chem. Phys.*, **12**, 2055–2076,
764 https://doi.org/10.5194/acp-12-2055-2012.
765
766 Cotton, W.R. , G.J. Tripoli, R.M. Rauber, and E.A. Mulvihill, 1986: Numerical simulation of
767 the effects of varying ice crystal nucleation rates and aggregation processes on orographic
768 snowfall, *J. Climate Appl. Meteorol.*, **25**, 1658-1680, doi.org/10.1175/1520-
769 0450(1986)025<1658:NSOTEO>2.0.CO;2
770
771 Chellini, G., R. Gierens, and S. Kneifel, 2022: Ice aggregation in low-level mixed-phase

772 clouds at a high Arctic site: Enhanced by dendritic growth and absent close to the melting
773 level. *J. Geophys. Res.: Atmos.*, **127**, e2022JD036860. doi: 10.1029/2022JD036860
774
775 de Boer, G., Eloranta, E. W., & Shupe, M. D. (2009). Arctic mixed-phase stratiform cloud
776 properties from multiple years of surface-based measurements at two high-latitude locations.
777 *Journal of the Atmos. Sci.*, ***66***(9), 2874–2887. https://doi.org/10.1175/2009JAS3029.
778
779 Dee D.P., and Coauthors, 2011: The ERA-Interim reanalysis: configuration and performance
780 of the data assimilation system, *Q.J.R. Meteorol. Soc*., **137**, 553-597, doi.org/10.1002/qj.828
781
782 Delanoë, J. ,and R. J. Hogan, 2010: Combined CloudSat-CALIPSO-MODIS retrievals of the
783 properties of ice clouds, *J. Geophys. Res.*, **115**, D00H29, doi: 10.1029/2009JD012346
784
785 Deshmukh, A., V. T. J. Phillips, A. Bansemer, S. Patade, and D. Waman, 2022: New
786 Empirical Formulation for the Sublimational Breakup of Graupel and Dendritic Snow, *J.*
787 *Atmos. Sci.*, **79**, 317–336, doi:10.1175/JAS-D-20-0275.1
788
789 Ebell, K., T. Nomokonova, M. Maturilli, and C. Ritter, 2020: Radiative Effect of Clouds at
790 Ny-Ålesund, Svalbard, as Inferred from Ground-Based Remote Sensing Observations, *J.*
791 *Appl. Meteor. Clim.*, **59**(1), 3-22, doi: 10.1175/JAMC-D-19-0080.1
792
793 Field., P., and Coauthors, 2017: Chapter 7: Secondary ice production - current state of the
794 science and recommendations for the future, Meteor. Monogr., **58**, 7.1–7.20 doi:
795 10.1002/2015GL065497

796 Gayet, J.-F., R. Treffeisen, A. Helbig, J. Bareiss, A. Matsuki, A. Herber, A. Schwarzenboeck,
797 2009: On the onset of the ice phase in boundary layer Arctic clouds, *J. Geophys. Res.*, **114**,
798 D19201, doi: 10.1029/2008jd011348

799 Georgakaki, P., G. Sotiropoulou, É. Vignon, A. C. Billault-Roux, A. Berne, and A. Nenes,
800 2022: Secondary ice production processes in wintertime alpine mixed-phase clouds, Atmos.
801 Chem. Phys., **22**, 1965–1988, doi: 10.5194/acp-22-1965-2022
802
803 Gettelman, A., and H. Morrison, 2015: Advanced Two-Moment Bulk Microphysics for

Global Models. Part I: Off-Line Tests and Comparison with Other Schemes, *J. Clim.*, **28**(3), 1268-1287, doi: 10.1175/JCLI-D-14-00102.1

Gossart, A., and Coauthors, 2017: Blowing snow detection from ground-based ceilometers: application to East Antarctica, The Cryosphere, **11**, 2755–2772, https://doi.org/10.5194/tc-11-2755-2017.

Hallett, J., and S. C. Mossop, 1974: Production of secondary ice particles during the riming process, *Nature*, **249**, 26–28, doi: 10.1038/249026a0

Hogan, R. J., M. P. Mittermaier, and A. J. Illingworth, 2006: The Retrieval of Ice Water Content from Radar Reflectivity Factor and Temperature and Its Use in Evaluating a Mesoscale Model, *J. Appl. Meteor. Clim.*, **45**(2), 301-317, doi: 10.1175/JAM2340.1

Hoose, C., J. E. Kristjánsson, J.-P. Chen, and A. Hazra, 2010: A classical-theory-based parameterization of heterogeneous ice nucleation by mineral dust, soot, and biological particles in a global climate model. *J. Atmos. Sci.*, **67**(8), 2483–2503, doi: 10.1175/2010JAS3425.1

Hoose, C., and O. Möhler, 2012: Heterogeneous ice nucleation on atmospheric aerosols: a review of results from laboratory experiments, *Atmos. Chem. Phys.*, **12**, 9817–9854, doi: 10.5194/acp-12-9817-2012

Illingworth, J., and Coauthors, 2007: Cloudnet, *Bull. Amer. Meteor. Soc.*, **88**(6), 883-898, doi: 10.1175/BAMS-88-6-883

Karlsson, L., R. Krejci, M. Koike, K. Ebell, and P. Zieger, 2021a: A long-term study of cloud residuals from low-level Arctic clouds, Atmos. Chem. Phys., **21**, 8933–8959, doi:10.5194/acp-21-8933-2021

Karlsson, L., R. Krejci, M. Koike, K. Ebell, and P. Zieger, 2021b: Arctic cloud and aerosol measurements from Zeppelin Observatory, Svalbard, November 2015 to February 2018. Dataset version 1. Bolin Centre Database. https://doi.org/10.17043/zeppelin-cloud-aerosol-1

Karrer, M., A. Seifert, D. Ori, and S. Kneifel, 2021: Improving the representation of aggregation in a two-moment microphysical scheme with statistics of multi-frequency Doppler radar observations, Atmos. Chem. Phys., **21**, 17133–17166, doi:10.5194/acp-21-17133-2021

Kato, S., and Coauthors, 2018: Surface Irradiances of Edition 4.0 Clouds and the Earth's Radiant Energy System (CERES) Energy Balanced and Filled (EBAF) Data Product, *Journal of Climate*, **31**(11), 4501-4527, doi: 10.1175/JCLI-D-17-0523.1

Keinert, A., D. Spannagel, T. Leisner, and A. Kiselev, 2020: Secondary Ice Production upon Freezing of Freely Falling Drizzle Droplets, *J. Atmos. Sci.*, **77**(8), 2959-2967, doi: 10.1175/JAS-D-20-0081.1

Kirkevåg, A., and Coauthors, 2018: A production-tagged aerosol module for Earth system models, OsloAero5.3 – extensions and updates for CAM5.3-Oslo, Geosci. Model Dev., **11**, 3945–3982, doi:10.5194/gmd-11-3945-2018.

Korolev, A., and T. Leisner, 2020: Review of experimental studies of secondary ice production, *Atmos. Chem. Phys.*, **20**, 11767–11797, doi: 10.5194/acp-20-11767-2020

Lauber, A., A. Kiselev, T. Pander, P. Handmann, and T. Leisner, 2018a: Secondary ice formation during freezing of levitated droplets, *J. Atmos. Sci.*, **75**, 2815–2826, doi: 10.1175/JAS-D-18-0052.1

Lamb, D. and J. Verlinde, 2011: Physics and Chemistry of Clouds. Cambridge University Press, Cambridge, doi: 10.1017/CBO9780511976377

Lawson, R. P, S. Woods, and H. Morrison., 2015: The microphysics of ice and precipitation development in tropical cumulus clouds. *J. Atmos. Sci.*, **72**, 2429–2445, doi:/10.1175/JAS-D-14-0274.1

Lloyd, G., and Coauthors, 2015: Observations and comparisons of cloud microphysical

properties in spring and summertime Arctic stratocumulus clouds during the ACCACIA campaign, *Atmos. Chem. Phys.*, **15**, 3719–3737, doi: 10.5194/acp-15-12953-2015

Löhnert, U., and S. Crewell, 2003: Accuracy of cloud liquid water path from ground-based microwave radiometry 1. Dependency on cloud model statistics, *Radio Sci.*, 38, 8041, doi:10.1029/2002RS002654, **3**, doi: 10.1029/2002RS002654

Luke, E.P., F. Yang, P. Kollias, A.M. Vogelmann, and M.,Maahn, 2021: New insights into ice multiplication using remote-sensing observations of slightly supercooled mixed-phase clouds in the Arctic. *Proceedings of the National Academy of Sciences,* **118**. doi: 10.1073/pnas.2021387118

Meyers, M. P., P. J. DeMott, and W.R. Cotton, 1992: New Primary Ice-Nucleation Parameterizations in an Explicit Cloud Model. *Journal of Applied Meteorology (1988-2005)*, **31**(7), 708–721, http://www.jstor.org/stable/26186583

Mizuno, H., 1990: Parameterization if the accretion process between different precipitation elements. *J. Meteor. Soc. Japan*, **57**, 273-281, doi: 10.2151/jmsj1965.68.3_395

Morrison, H., J.A. Curry, V.I. Khvorostyanov, 2005: A New Double-Moment Microphysics Parameterization for Application in Cloud and Climate Models. Part I: Description, *Atmos. Sci.,* **62**, 3683-3704, doi: 10.1175/JAS3446.1

Morrison, H., G. De Boer, G. Feingold, J. Harrington, M.D. Shupe, and K. Sulia, 2012: Resilience of persistent Arctic mixed-phase clouds, Nat. Geosci., **5**, 11–17, doi: 10.1038/ngeo1332

Murray, B. J., K. S. Carslaw, and P. R. Field, 2021: Opinion: cloud- phase climate feedback and the importance of ice- nucleating particles, Atmos. Chem. Phys., **21**(2), 665– 679, doi: 10.5194/acp-21-665-2021

Naakka, T., T. Nygård, and T. Vihma, 2018: Arctic Humidity Inversions: Climatology and Processes. *J. Climate*, **31**, 3765–3787, doi: 10.1175/JCLI-D-17-0497.1.

902 Nomokonova, T., K. Ebell, U,.Löhnert, M. Maturilli, C. Ritter, and E. O'Connor, 2019:
903 Statistics on clouds and their relation to thermodynamic conditions at Ny-Ålesund using
904 ground-based sensor synergy, Atmos. Chem. Phys., **19**, 4105–4126,
905 https://doi.org/10.5194/acp-19-4105-2019.
906
907 Nomokonova, T., C. Ritter, and K. Ebell, 2019a: Liquid water path of HATPRO microwave
908 radiometer at AWIPEV, Ny-Ålesund (2016). PANGAEA, doi: 10.1594/PANGAEA.902096
909
910 Nomokonova, T., C. Ritter, and K. Ebell, 2019b: Liquid water path of HATPRO microwave
911 radiometer at AWIPEV, Ny-Ålesund (2017). PANGAEA, doi: 10.1594/PANGAEA.902098
912
913 Nomokonova, T., C. Ritter, and K. Ebell, 2019c: Liquid water path of HATPRO microwave
914 radiometer at AWIPEV, Ny-Ålesund (2017). PANGAEA, doi: 10.1594/PANGAEA.902099
915
916 Nomokonova, T., and K. Ebell, 2019d: Cloud microphysical properties retrieved from
917 ground-based remote sensing at Ny-Ålesund (10 June 2016 - 8 October 2018). University of
918 Cologne, PANGAEA, doi: 10.1594/PANGAEA.898556
919
920 Nomokonova, T., C. Ritter, and K. Ebell, 2019e: Temperature profile of HATPRO
921 microwave radiometer at AWIPEV, Ny-Ålesund (2016). PANGAEA, doi:
922 10.1594/PANGAEA.902145
923
924 Nomokonova, T., C. Ritter, and K. Ebell, 2019f: Temperature profile of HATPRO microwave
925 radiometer at AWIPEV, Ny-Ålesund (2017). PANGAEA, doi: 10.1594/PANGAEA.902146
926
927 Nomokonova, T., C. Ritter, and K. Ebell, 2019g: Temperature profile of HATPRO
928 microwave radiometer at AWIPEV, Ny-Ålesund (2018). PANGAEA, doi:
929 10.1594/PANGAEA.902147
930
931 Nomokonova, T., C. Ritter, and K. Ebell, 2019h: Integated water vapor of HATPRO
932 microwave radiometer at AWIPEV, Ny-Ålesund (2016). PANGAEA, doi:
933 10.1594/PANGAEA.902140
934

935 Nomokonova, T., C. Ritter, and K. Ebell, 2019i: Integated water vapor of HATPRO
936 microwave radiometer at AWIPEV, Ny-Ålesund (2017). PANGAEA, doi:
937 10.1594/PANGAEA.902142
938
939 Nomokonova, T., C. Ritter, and K. Ebell, 2019j: Integated water vapor of HATPRO
940 microwave radiometer at AWIPEV, Ny-Ålesund (2018). PANGAEA, doi:
941 10.1594/PANGAEA.902143

942 Oraltay, R., and J. Hallett, 1989: Evaporation and melting of ice crystals: A laboratory
943 study. *Atmos. Res.*, **24**, 169–189, doi:10.1016/0169-8095(89)90044-6

944 Pasquier, J. T., and Coauthors, 2022: Conditions favorable for secondary ice production in
945 Arctic mixed-phase clouds, Atmos. Chem. Phys. Discuss. [preprint],
946 https://doi.org/10.5194/acp-2022-314
947
948 Passarelli, R. E., 1978: An Approximate Analytical Model of the Vapor Deposition and
949 Aggregation Growth of Snowflakes, *J. Atmos. Sci.*, **35**(1), 118-124, doi: 0.1175/1520-
950 0469(1978)035<0118:AAAMOT>2.0.CO;2
951
952 Phillips, V. T. J., M. Formenton, A. Bansemer, I. Kudzotsa, and B. Lienert, 2015). A
953 Parameterization of Sticking Efficiency for Collisions of Snow and Graupel with Ice Crystals:
954 Theory and Comparison with Observations, *J. Atmos. Sci.*, **72**(12), 4885-4902.
955
956 Phillips, V. T. J, J. I. Yano, A. Khain, 2017a: Ice multiplication by breakup in ice-ice
957 collisions. Part I: Theoretical formulation, *J. Atmos. Sci.*, **74**, 1705 1719, doi: 10.1175/JAS-
958 D-16-0224.1
959
960 Phillips, V. T. J., J. I. Yano, M. Formenton, E. Ilotoviz, V. Kanawade, I. Kudzotsa, J. Sun, A.
961 Bansemer, A.G. Detwiler, A. Khain, and S.A., Tessendorf, 2017b: Ice multiplication by
962 breakup in ice-ice collisions. Part II: Numerical simulations, J. Atmos. Sci., **74**, 2789–
963 2811,doi: 10.1175/JAS-D-16-0223.1
964
965 Phillips, V. T. J., S. Patade, J. Gutierrez, and A. Bansemer, 2018: Secondary Ice Production
966 by Fragmentation of Freezing Drops: Formulation and Theory, *J. Atmos. Sci.*, **75**(9), 3031-

3070, doi:10.1175/JAS-D-17-0190.1

Rangno, A.L., and P.V. Hobbs, 2001: Ice particles in stratiform clouds in the Arctic and possible mechanisms for the production of high ice concentrations, *J. Geophys. Res.*, **106**, 15065–15075, doi: 10.5194/acp-19-5293-2019

Reisner, J., R. M. Rasmussen, and R. T. Bruintjes, 1998: Explicit forecasting of supercooled liquid water in winter storms using the MM5 mesoscale model, *Quart. J. Roy. Meteor. Soc.*, **124**(548), 1071-1107, doi: 10.1002/qj.49712454804

Schmeisser, L., and Coauthors, 2018: Seasonality of aerosol optical properties in the Arctic, Atmos. Chem. Phys., 18, 11599–11622, https://doi.org/10.5194/acp-18-11599-2018.

Schwarzenboeck, A., V. Shcherbakov, R. Lefevre, J. F. Gayet, Y. Pointin, and C. Duroure, 2009: Indications for stellar-crystal fragmentation in Arctic clouds, Atmos. Res., **92,** 220–228, doi: 10.1016/j.atmosres.2008.10.002

Seinfeld J. H., and Coauthors, 2016: Improving our fundamental understanding of the role of aerosol-cloud interactions in the climate system. *Proc. Natl. Acad. Sci. USA*, **113**(21), 5781–5790, doi:10.1073/pnas.1514043113

Seland, Ø., and Coauthors, 2020: Overview of the Norwegian Earth System Model (NorESM2) and key climate response of CMIP6 DECK, historical, and scenario simulations, *Geosci. Model Dev.*, **13**, 6165–6200, doi: 10.5194/gmd-13-6165-2020

Shaw, J., Z. McGraw, O. Bruno, T. Storelvmo, and S. Hofer, 2022: Using satellite observations to evaluate model microphysical representation of Arctic mixed-phase clouds. *Geophysical Research Letters*, **49**, e2021GL096191. doi: 10.1029/2021GL096191

Shupe, M. D, S. Y. Matrosov, and T. Uttal, 2006: Arctic Mixed-Phase Cloud Properties Derived from Surface-Based Sensors at SHEBA, *J. Atmos. Sci.*, **63**(2), 697-711, doi: 10.1175/JAS3659.1

Shupe, M. D., V. P. Walden, E. Eloranta, T. Uttal, J. R. Campbell, S. M. Starkweather, and M. Shiobara, 2011: Clouds at Arctic at- mospheric observatories. Part I: Occurrence and macro- physical properties. J. Appl. Meteor. Climatol., **50**, 626–644, doi:10.1175/2010JAMC2467.1.

Sledd, A., and T. L'Ecuyer, 2021: Uncertainty in Forced and Natural Arctic Solar Absorption Variations in CMIP6 Models, *Journal of Climate*, **34(**3), 931-948. 10.1175/JCLI-D-20-0244.1

Storelvmo, T., 2017: Aerosol Effects on Climate via Mixed-Phase and Ice Clouds. *Annual Review of Earth and Planetary Sciences,* **45**, 199-222, doi:10.1146/ANNUREV-EARTH-060115-012240

Sotiropoulou, G., S. Sullivan, J. Savre, G. Lloyd, T. Lachlan-Cope, A. M. L. Ekman, and A. Nenes, 2020: The impact of secondary ice production on Arctic stratocumulus, Atmos. Chem. Phys., **20**, 1301–1316, doi: 10.5194/acp-20-1301-2020

Sotiropoulou, G., É. Vignon, G. Young, H. Morrison, S. J. O'Shea, T. Lachlan-Cope, A. Berne, and A. Nenes, 2021a: Secondary ice production in summer clouds over the Antarctic coast: an underappreciated process in atmospheric models, Atmos. Chem. Phys., **21**, 755–771, doi: 10.5194/acp-21-755-2021

Sotiropoulou, G., L. Ickes, A. Nenes, A., and A.M.L. Ekman, 2021b: Ice multiplication from ice–ice collisions in the high Arctic: sensitivity to ice habit, rimed fraction, ice type and uncertainties in the numerical description of the process, Atmos. Chem. Phys., **21**, 9741–9760, doi: 10.5194/acp-21-9741-2021.

Sullivan, S. C., A. Kiselev, T. Leisner, C. Hoose, ans A. Nenes, 2018: Initiation of secondary ice production in clouds, *Atmos. Chem. Phys.*, **18**, 1593–1610, doi: 10.5194/acp-18-1593-2018

Takahashi, T., Y. Nagao, and Y. Kushiyama, 1995: Possible high ice particle production during graupel-graupel collisions, J. Atmos. Sci., **52**, 4523–4527

Tan, I., and T. Storelvmo, 2019: Evidence of strong contributions from mixed-phase clouds to Arctic climate change. *Geophys. Res. Let.*, **46**, 2894– 2902, doi: 10.1029/2018GL081871

Thomas, M. A., A. Devasthale, T. L'Ecuyer, S. Wang, T. Koenigk and K. Wyser, 2019: Snowfall distribution and its response to the Arctic Oscillation: an evaluation of HighResMIP models in the Arctic using CPR/CloudSat observations, Geosci. Model Dev., **12**, 3759–3772, doi:10.5194/gmd-12-3759-2019

Vardiman, L., 1978: The generation of secondary ice particles in clouds by crystal-crystal collision, J. *Atmos. Sci.*, **35**, 2168–2180, doi: 0.1175/1520-0469(1978)035<2168:TGOSIP>2.0.CO;2,

Vignesh, P. P., J. H. Jiang, P. Kishore, H. Su, T. Smay, N. Brighton, and I. Velicogna, 2020: Assessment ofCMIP6 cloud fraction and comparisonwith satellite observations.Earth and Space Science, **7**, e2019EA000975. doi: 10.1029/2019EA000975

Wang, Y., X. Liu, C. Hoose, C., and B. Wang, 2014: Different contact angle distributions for heterogeneous ice nucleation in the Community Atmospheric Model version 5. *Atmos. Chem. Phys.*, **14**(19), 10411–10430, doi: 10.5194/acp-14-10411-2014

Wex, H., and Coauthors, 2019: Annual variability of ice-nucleating particle concentrations at different Arctic locations, *Atmos. Chem. Phys.*, **19**, 5293-5311, doi:10.5194/acp-19-5293-2019

Wielicki, B. A., B. R. Barkstrom, E. F. Harrison, R. B. III Lee, G. L. Smith, and J. E. Cooper, 1996: Clouds and the Earth's Radiant Energy System (CERES): An Earth Observing System Experiment, *Bull. Amer. Meteorol. Soc*., **77**(5), 853-868, doi: ulletin of the American Meteorological Society, **77**(5), 853-868, doi: 10.1175/1520-0477(1996)077<0853:CATERE>2.0.CO;2.

Young, K. C., 1974: The Role of Contact Nucleation in Ice Phase Initiation in Clouds, *Journal of Atmospheric Sciences*, **31**(3), 768-776.

Zelinka, M. D., and Coauthors, 2020: Causes of higher climate sensitivity in CMIP6 models. Geophys. Res. Lett., **47**, e2019GL085782, doi:10.1029/2019GL085782.

Zhao, X., X. Liu, V. T. J. Phillips, and S. Patade, 2021: Impacts of secondary ice production on Arctic mixed-phase clouds based on ARM observations and CAM6 single-column model simulations, *Atmos. Chem. Phys.*, **21**, 5685–5703, doi: 10.1029/2021GL092581

Zhao, X., and X. Liu, 2021: Global importance of secondary ice production. *Geophys. Res. Let.*, **48**, e2021GL092581, doi: 10.1029/2021GL092581

Zhao, X., and X. Liu, 2022: Relative importance and interactions of primary and secondary ice production in the Arctic mixed-phase clouds*, Atmos. Chem. Phys.*, **22**, 2585–2600, doi: 10.5194/acp-2021-686